Deposition of an oxomanganese water oxidation catalyst on TiO_2 nanoparticles: computational modeling, assembly and characterization†

Gonghu Li, Eduardo M. Sproviero, Robert C. Snoeberger III, Nobuhito Iguchi, James D. Blakemore, Robert H. Crabtree,* Gary W. Brudvig* and Victor S. Batista*

Received 22nd October 2008, Accepted 4th December 2008
First published as an Advance Article on the web 12th January 2009
DOI: 10.1039/b818708h

Inexpensive water oxidation catalysts are needed to develop photocatalytic solar cells that mimic photosynthesis and produce fuel from sunlight and water. This paper reports the successful attachment of a dinuclear di-μ-oxo manganese water oxidation catalyst $[H_2O(terpy)Mn^{III}(\mu\text{-}O)_2Mn^{IV}(terpy)H_2O](NO_3)_3$ (**1**, terpy = 2,2′:6′2″-terpyridine) onto TiO_2 nanoparticles (NPs) *via* direct adsorption, or *in situ* synthesis. The resulting surface complexes are characterized by EPR and UV-visible spectroscopy, electrochemical measurements and computational modeling. We conclude that the mixed-valence (III,IV) state of **1** attaches to near-amorphous TiO_2 NPs by substituting one of its water ligands by the TiO_2 NP, as suggested by low-temperature (7 K) EPR data. In contrast, the analogous attachment onto well-crystallized TiO_2 NPs leads to dimerization of **1** forming Mn(IV) tetramers on the TiO_2 surface as suggested by EPR spectroscopy and electrochemical studies.

1. Introduction

Solar energy is a vast potential source of renewable energy but we still lack cheap, efficient and robust solar cells. For large-scale applications, it is important to avoid rare elements, such as ruthenium needed in Grätzel cells. Beyond electrical energy production, it should be possible to mimic photosynthesis and produce fuel from sunlight and water by incorporating a water oxidation catalyst into a solar cell.[1] In this paper, we report the attachment of a dimanganese water oxidation catalyst on TiO_2 nanoparticles (NPs). We describe the synthesis and characterization based on computational modeling, UV-visible and electron paramagnetic resonance (EPR) spectroscopy, and electrochemical measurements.

Oxide semiconductors have been widely explored as catalysts for H_2 production, based on solar water splitting.[2] In particular, TiO_2-based materials have been particularly attractive as photocatalysts,[3] largely because the TiO_2 band edges bracket the redox potential for water splitting.[4] However, TiO_2 has a relatively large band-gap and its direct photoactivation requires UV light ($\lambda < 400$ nm), accounting for only less than 4% of the natural sunlight spectrum.[5] While it is possible to extend the absorption edges of TiO_2 into the visible-light region,[5–7] multi-photon activation would still be required to accumulate the energy needed for water splitting. Several other composite semiconductors are also visible light catalysts for water splitting,[8,9] but their efficiencies are still too low. Common challenges include the recombination of the photogenerated electron-hole pairs, and the usual weak photocatalytic activity of semiconductor surface sites.

Surface functionalization of TiO_2 NPs has been extensively investigated within the context of Grätzel cells as the most successful strategy for maximizing light-harvesting with wide band-gap semiconductors.[10,11] Dye-molecules attached to TiO_2 surfaces shift the absorption threshold to the visible light region and efficiently inject electrons into the semiconductor conduction band upon visible photoexcitation. However, the photo-generated holes (h^+) are typically localized in the oxidized adsorbate molecules with a potential that is insufficient to oxidize water.

Department of Chemistry, Yale University, P.O. Box 208107, New Haven, CT, 06520-8107, USA. E-mail: robert.crabtree@yale.edu; gary.brudvig@yale.edu; victor.batista@yale.edu

† Electronic supplementary information (ESI) available: Optimized structure of complex **1**, TEM images of TiO_2 NPs, EPR spectra of **1**-D70 and isolated **1**, and UV-visible spectra of complexes **1** and **2**. See DOI: 10.1039/b818708h

Broader context

In Nature, the production of O_2 by oxidizing water is catalyzed by an Mn_4Ca inorganic unit in the oxygen-evolving complex of photosystem II. Heterogeneous arrays consisting of a light harvester, a water oxidation catalyst, and an electron acceptor have been considered a promising approach for artificial photosynthesis. In this study, we deposited a di-nuclear manganese water oxidation catalyst on the surfaces of TiO_2 nanoparticles, which have shown to be efficient electron acceptors. The synthesized materials were thoroughly characterized with a variety of techniques and computational modeling. Both experimental and theoretical studies indicate the successful surface immobilization of an oxomanganese water oxidation catalyst. This approach could be utilized to build an artificial photosynthetic system, in which the oxomanganese catalyst facilitates water oxidation and the TiO_2 surface collects photogenerated electrons for solar hydrogen production.

Therefore, while dye-sensitized solar cells may be efficient for light harvesting and photon-to-electricity conversion, they do not necessarily lead to solar water splitting.

Water oxidation into O_2, protons and electrons is a four electron oxidation reaction,[12]

$$2H_2O \rightarrow O_2 + 4H^+ + 4e^-,$$

often catalyzed by sacrificial electron acceptors capable of accumulating four oxidizing equivalents (h^+'s). A variety of water oxidation catalysts have been synthesized and many of them have been coupled with chromophores in artificial photosynthetic assemblies.[13–17] Most of these catalysts are polynuclear transition metal coordination complexes of Mn, Ru, Ir and Co. For scalability, inexpensive metals such as Mn and Co are preferred over Ru and Ir. In Nature, water oxidation is catalyzed by an oxomanganese complex and involves an oxidation mechanism that we are beginning to understand at the molecular level.[18,19] Several Mn complexes have been reported to be water oxidation catalysts,[20,21] including our own di-μ-oxo Mn dimer $[H_2O(terpy)Mn^{III}(\mu\text{-}O)_2Mn^{IV}(terpy)H_2O](NO_3)_3$ (**1**, terpy = 2,2′:6′2″-terpyridine) that is an efficient catalyst for O_2 evolution[22,23] when activated with a primary oxidant (*e.g.*, oxone).

Complex **1** is thought to be biomimetic since some of its structural and mechanistic features are similar to those of the photosynthetic reaction center.[18,24–27] While the catalytic mechanism of water oxidation based on complex **1** is not yet established,[26] it is thought to involve the formation of a high-valent oxyl radical species Mn^{IV}–O$^\bullet$ species according to the following reactions:

$$[H_2O(terpy)Mn^{III}(\mu\text{-}O)_2Mn^{IV}(terpy)H_2O]^{3+} \rightarrow [H_2O(terpy)Mn^{IV}(\mu\text{-}O)_2Mn^{IV}(terpy)OH]^{3+} + H^+ + e^-$$

$$[H_2O(terpy)Mn^{IV}(\mu\text{-}O)_2Mn^{IV}(terpy)OH]^{3+} \rightarrow [H_2O(terpy)Mn^{IV}(\mu\text{-}O)_2Mn^{IV}\text{–}O^\bullet(terpy)]^{3+} + H^+ + e^-$$

$$[H_2O(terpy)Mn^{IV}(\mu\text{-}O)_2Mn^{IV}\text{–}O^\bullet(terpy)]^{3+} + H_2O \rightarrow [Mn^{II}\cdots Mn^{III}] + O_2 + 2H^+$$

As indicated above in the last step of the postulated mechanism, the oxyl radical is susceptible to nucleophilic attack by a water molecule, forming a hydroperoxo intermediate that rapidly decomposes into O_2 upon deprotonation. As observed in ref. 22 and 23, one of the oxygen atoms in O_2 often comes from the primary oxidant (H_2SO_5), forming O^{16}–O^{18} when reacting with H_2O^{18}, although a minority component involves O^{18}–O^{18}. For heterogeneous applications, it is, therefore, important to investigate first whether complex **1** can be anchored to a sacrificial electron acceptor and whether O_2 evolution can be induced by activation of the resulting surface complex with a primary oxidant.

A few studies have already investigated the catalytic and photochemical properties of oxomanganese water oxidation catalysts on solid supports. Yagi and co-workers deposited complex **1** on clay materials and saw catalytic oxygen evolution from Ce^{4+} as the single-electron oxidant.[28,29] They suggested that complex **1** was autoxidized to the (IV,IV) state on kaolin, which is then capable of catalyzing single-electron water oxidation.[28] They later found that adsorption on clay suppressed the decomposition of **1** to MnO_4^- and suggested that water oxidation is facilitated by the cooperation of two equivalents of **1**.[29] Recently, Weare *et al.*[30] reported a nanostructured assembly in which a related oxomanganese complex, $[(bpy)_2Mn^{III}(\mu\text{-}O)_2Mn^{IV}(bpy)_2](NO_3)_3$ (bpy = 2,2′-bipyridine), was coupled to single Cr^{VI} charge-transfer chromophore in the channels of nanoporous silica. FT-Raman and EXAFS studies demonstrated that visible light induced electron transfer from the $Mn^{III}(\mu\text{-}O)_2Mn^{IV}$ core to Cr^{VI} forming $Mn^{IV}(\mu\text{-}O)_2Mn^{IV}$ and Cr^{V}.[30] In this study, we build upon earlier work[31,32] and we focus on the attachment of complex **1** onto TiO_2 NPs and on the characterization of the resulting surface complexes by computational studies, UV-visible and EPR spectroscopy, and electrochemical measurements.

2. Experimental procedures

All reagents and solvents were purchased from Aldrich and used without further purification. MilliQ water was used to make all of the aqueous solutions.

2.1. Materials synthesis

2.1.1. Synthesis of $[(H_2O)(terpy)Mn^{III}(\mu\text{-}O)_2Mn^{IV}(terpy)(H_2O)](NO_3)_3$ (1). Following the method of Chen and co-workers,[33] the precursor of complex **1**, $Mn^{II}(terpy)Cl_2$, was obtained by reaction of terpy with an excess of $MnCl_2$. Complex **1** was then obtained at 0 °C using oxone ($2KHSO_5\cdot KHSO_4\cdot K_2SO_4$) as the oxidant.[33]

2.1.2. Synthesis of TiO_2 nanoparticles. A commercially available TiO_2 sample, Degussa P25, was used as received. TiO_2 NPs were also synthesized by a modified solvothermal method.[34] 10 ml of Ti(IV) isopropoxide was dissolved in 200 ml of dichloromethane in a flask under dry nitrogen. Six milliliters of 0.1 M HCl solution was then added dropwise to the solution. After stirring for 90 min at room temperature, the resulting mixture was refluxed for 24 h with stirring. The resulting NPs were recovered by solvent evaporation followed by washing with copious water and drying at room temperature. Some samples of the resulting TiO_2 powder were sintered at 450 °C to improve crystallinity. The synthetic materials with and without thermal treatment at 450 °C are denoted "D450" and "D70", respectively.

2.1.3. Deposition of 1 on TiO_2. Complex **1** was deposited on the surface of TiO_2 NPs by one of two methods. In direct adsorption, 1.2 μmol of complex **1** and 20 mg of TiO_2 NPs were mixed in water at room temperature. In the *in situ* synthesis, 2.4 μmol $Mn^{II}(terpy)Cl_2$ was mixed with 20 mg TiO_2 in water before adding an oxone solution at room temperature. In both methods, the resulting mixture was stirred at room temperature for 90 min. Functionalized TiO_2 NPs were washed with 1.5 ml H_2O 3 times before recovery by centrifugation at 6000 rpm. Subsequent characterization and testing indicated that the two different preparative methods led to an essentially identical product (denoted "**1**–TiO_2").

2.2. Materials characterization

2.2.1. Powder X-Ray diffraction (XRD). The XRD data were recorded on a Bruker-AXS D8 Focus diffractometer ($\lambda = 1.5418$ Å, Cu Kα radiation, step time 1 s) over the range of $20° < 2\theta < 60°$. The step sizes were 0.05° and 0.02° for P25 and synthetic NPs, respectively.

2.2.2. EPR spectroscopy. Perpendicular-mode EPR spectra were recorded on an X-band Bruker Biospin/ELEXSYS E500 spectrometer equipped with a SHQ cavity and an Oxford ESR-900 liquid helium cryostat. All spectra were collected on water-dispersed samples in 5 mm OD quartz EPR tubes. The samples were purged with nitrogen and frozen in liquid nitrogen prior to recording spectra at 7 K. A high-intensity illuminator (Fiber-Lite Series 180, Dolan-Jenner Industries, Inc.) equipped with a fiber optic light guide, which only transmits light with wavelengths greater than 425 nm, was used as the visible light source in photochemical studies.

2.2.3. UV-visible spectra. Thin films of TiO_2 NPs were prepared on microscopic slides by doctor-blading and were used to collect spectra with a Varian Cary 3 spectrophotometer in diffuse reflectance geometry.[31] The baseline spectrum of the microscope slide, which only absorbs at wavelengths less than 350 nm, was always subtracted.

2.2.4. Electrochemical studies. Electrochemical measurements were made on an EG&G Princeton Applied Research Model 273 potentiostat/galvanostat using a standard three-electrode system. A platinum wire was used as the counter electrode, and a standard calomel electrode (SCE) was used as the reference electrode (NHE *vs.* SCE: +241 mV). The working electrodes were made from fluorine-doped tin oxide conducting glasses (FTO, Hartford Glass Co., Inc.), which were coated with TiO_2 NPs by doctor-blading. The TiO_2/FTO electrodes were sintered at 450 °C for 2 h and were washed with water immediately before running the electrochemical measurements. Experiments were carried out in unbuffered aqueous solutions containing 0.1 M KNO_3 as the supporting electrolyte.

2.2.5. Elemental analysis. All samples were analyzed on a Costech ECS 4010 elemental analyzer (Costech Analytical Technologies, Valencia, CA) coupled to a ThermoFinnigan DeltaPLUS Advantage stable isotope mass spectrometer (Thermo Scientific, Boca Raton, FL), with both controlled by the Thermo's Isodat 2.0 software. In a typical run, a dried TiO_2 sample (0.5–1.0 mg) was sealed in a tin capsule and loaded into the autosampler. Control experiments were run using pure TiO_2 materials and powdered complex **1**, and the results were calibrated with the house standard (standard cocoa powder, 4.15% N; 48.7% C). The output of the elemental analyzer, the N_2 and the CO_2 from N and C on TiO_2 surfaces, was sampled by the mass spectrometer.

2.3. Oxygen evolution assay

Using Ce^{4+} as the oxidant, oxygen evolution from aqueous solutions of **1**–TiO_2 dispersed in water was measured at 298 K by an oxygen probe (Clark electrode) connected to a YSI 5300A oxygen monitor with digital readout, interfaced to a computer for data logging.[35] The sample chamber was maintained at 25 °C with a circulating water bath. The instrument readout was calibrated against air-saturated distilled water kept stirred in the air-tight sample chamber under the Clark electrode. In a typical run, 3 μmol **1** and 50 mg TiO_2 were mixed in water and stirred at room temperature for 90 min. The resulting **1**–TiO_2 was then washed with water to remove excess **1** and was dispersed in 4 ml water in the sample chamber. After allowing time for equilibration and ensuring a constant baseline reading, 50 μL of an aqueous solution of 2 M ceric ammonium nitrate was introduced into the sample chamber.

3. Computational analysis

This section describes the computational methodology, including the preparation of structural models, the description of the Quantum Mechanics/Molecular Mechanics (QM/MM) hybrid methods, the methodology applied for simulations of UV-visible spectra, and the calculation of binding enthalpies. The results and discussion, with an emphasis on mechanistic implications, are presented in Section 4.

3.1. Molecular models

3.1.1. TiO_2 anatase nanoparticles. Precursor structural models of TiO_2 anatase NPs were obtained by DFT geometry optimization, starting with the crystal structure of bulk anatase. Model NPs, composed of complex **1** attached onto the (101) surface of anatase, were described by 32 [TiO_2] units with dimensions $1.0 \times 1.5 \times 3.1$ nm along the [−101], [010] and [101] directions, respectively. Periodic boundary conditions were imposed with a vacuum spacer between slabs, making negligible the interaction between distinct surfaces in the infinitely periodic model system. The surface dangling bonds were saturated with capping hydrogen atoms to quench the formation of surface states and avoid unphysical low coordination numbers. The DFT geometry relaxation was performed by using the Vienna Ab-initio Simulation Package (VASP/VAMP) implementing the PW91/GGA approximation in a plane-wave basis, and using ultrasoft Vanderbilt pseudopotentials to describe the ionic interactions. A wavefunction cutoff of 400 eV was used in all calculations as well as a single Gamma point k-point sampling, due to the large size of the supercell. The Kohn–Sham (KS) Hamiltonian was projected onto a plane-wave basis set and high-efficiency iterative methods were implemented to obtain the KS eigenstates and eigenvalues. Self-consistency was accelerated by means of efficient charge density mixing schemes.

3.1.2. TiO_2 anatase nanoparticles functionalized with 1. The functionalized TiO_2 model includes complex **1** attached onto a pristine TiO_2 surface. Molecular models of **1** are based on the X-ray atomic coordinates obtained from the Cambridge Crystallographic Data Center (CCDC) with reference code FIQFIU,[22] and further optimized at the DFT/B3LYP level of theory (see Fig. S1†).[36]

The reduced models included **1** adsorbed onto 15 [TiO_2] units and capped with terminal OH fragments, where the positions of

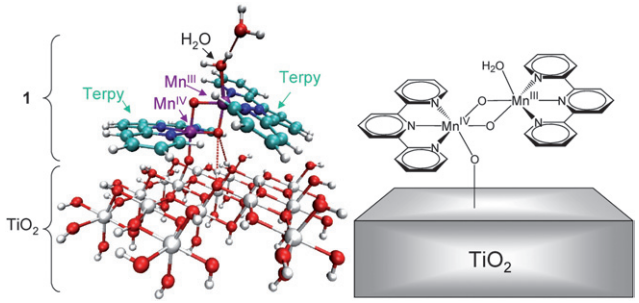

Fig. 1 Left panel: DFT/QM-QMM model of the Mn complex **1** anchored to a TiO_2–NP. A water ligand is exchanged by the NP and remains hydrogen-bonded to the other water ligand to allow for calculations of binding enthalpies (see text for details). Color scheme: C (light-blue), H (white), Mn (purple), N (blue), O (red), Ti (gray). **Right panel:** Schematic representation of the **1**–TiO_2.

the O atoms in the capping fragments were constrained to their corresponding positions in the 32 [TiO_2] unit precursor structure. To dock the complex to the surface, we assumed that one of the two water ligands is exchanged by the TiO_2 NP, leaving the Mn dimer immobilized on the surface by a single oxo bridge and hydrogen bonding interactions. The exchanged water molecule is stabilized by hydrogen bonding to the other water molecule in the complex. The orientation of the resulting complex adsorbate (Fig. 1), relative to the surface, was obtained by energy minimization at the DFT QM/MM level of theory.

3.2. QM/MM hybrid approach

QM/MM computations are based on the two-layer ONIOM electronic-embedding (EE) link-hydrogen atom approach[37] as implemented in Gaussian 03.[38] The ONIOM-EE method is applied by partitioning the system, according to a reduced high-level molecular domain (X layer) that includes complex **1**, its terpy ligands and water molecules (the model system). The rest of the system (Y layer) includes the TiO_2 surface and is described at the molecular mechanics level. The ONIOM QM/MM methodology could be efficiently applied, as in previous studies of the multiple nuclear transition metal compounds, only after obtaining high-quality initial-guess states for the cluster of Mn ions (the model system) according to ligand field theory[39] as implemented in Jaguar 5.5.[40] The resulting combined approach exploits important capabilities of ONIOM, including both the link-hydrogen atom scheme for efficient and flexible definitions of QM layers and the possibility of modeling open-shell systems by performing unrestricted DFT (*i.e.* UB3LYP) calculations.

The total energy E of the system is obtained at the ONIOM-EE level from three independent calculations as follows,

$$E = E^{\mathrm{MM,X+Y}} + E^{\mathrm{QM,X}} - E^{\mathrm{MM,X}}$$

where $E^{\mathrm{MM,X+Y}}$ is the energy of the complete system computed at the molecular-mechanics level of theory, while $E^{\mathrm{QM,X}}$ and $E^{\mathrm{MM,X}}$ correspond to the energy of the reduced system computed at the QM and MM levels of theory, respectively. Electrostatic interactions between the layers X and Y are included in the calculation of both $E^{\mathrm{QM,red}}$ and $E^{\mathrm{MM,red}}$ at the quantum mechanical and molecular mechanical levels, respectively. Therefore, the electrostatic interactions computed at the MM level in $E^{\mathrm{MM,red}}$ and $E^{\mathrm{MM,full}}$ cancel. The resulting QM/MM evaluation of the total energy at the ONIOM-EE level includes a quantum mechanical description of polarization of the reduced system due to the electrostatic influence of the surrounding environment.

The efficiency of the QM/MM calculations is optimized by using a combination of basis sets for the QM layer, including the lacvp basis set for Mn ions in order to consider non-relativistic electron core potentials, the 6-31G(d) basis set for O in order to include polarization functions on bridging oxides, and the 6-31G basis set for the N and 3-21G basis set for C and H atoms in the QM layer. Such a choice of basis set has been validated through extensive benchmark calculations on high-valent manganese complexes.[36] The molecular structure beyond the QM layer is described by the UFF MM force field.[41] Charges of the molecular mechanics layer were computed by using the Charge Equilibration (QEq) method for molecular dynamics simulations,[42] which is consistent with the UFF force field.

The model TiO_2 slab, with dimensions 1.5 nm × 1.5 nm × 0.4 nm, includes 113 atoms and corresponds to the smallest possible cluster that provides a converged value of the binding affinity of the complex. Its fully relaxed configuration is obtained by energy minimization at the ONIOM-EE (UHF B3LYP/lacvp (Mn),6-31G* (O),6-31G(N),3-21G (C and H) UFF level of theory, subject to the constraint of fixed OH capping fragments. The electronic state of the surface adsorbate complex involves high-spin anti-ferromagnetic couplings between Mn centers. The resulting optimized structures are analyzed and evaluated not only on the basis of the total energy of the system but also as compared to structural, electronic, and mechanistic features that should be consistent with experimental data.

3.3. Binding enthalpies

DFT QM/MM calculations of binding energies are based on the fully optimized configurations of the structural models (a), (b) and (c) shown in Scheme 1, modeled as described in Sections. 3.1 and 3.2. The binding enthalpy $\Delta H = E(\mathrm{a}) - [E(\mathrm{b}) + E(\mathrm{c})]$ is obtained by computing the energy difference between the energy of the whole system E(a) (*i.e.*, the energy of **1** adsorbed on TiO_2) and the sum of the energies of **1** [*i.e.*, E(c)] and TiO_2 [*i.e.*, E(b)]. Complex **1** adsorbed on the TiO_2 surface includes an additional water molecule, as shown in Fig. 1, that serves to conserve the total number of atoms in the QM layers of reactants and products. Upon detachment of the complex from the surface, the additional water molecule forms an OH ligand to Mn^{IV} and the capping H of the TiOH fragment on the attachment site of the TiO_2 surface (see Scheme 1).

3.4. Simulations of UV-visible spectra

The simulations of UV-visible spectra are based on electronic structure calculations of the TiO_2 anatase nanoparticles functionalized with **1**, as previously reported.[31] The calculations are based on a tight-binding model Hamiltonian of the complete supercell **1**–TiO_2, gained from the Extended-Hückel (EH) semi-empirical approach for electronic structure calculations. The EH method requires a relatively small number of transferable parameters and is capable of providing semiquantitative

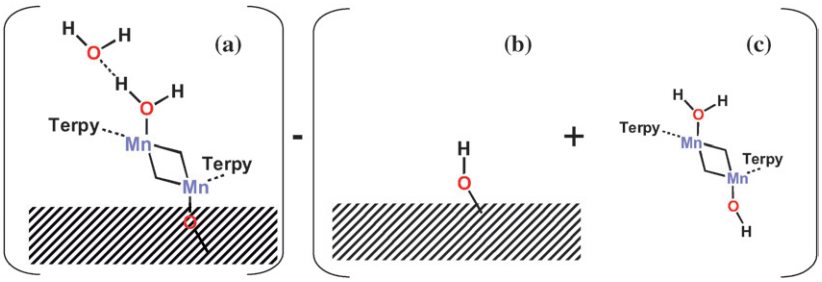

Scheme 1 Binding energies are calculated as the difference between the extrapolated energy of the whole system (a), which includes the TiO_2 surface, the terpy complex **1** and a substrate water molecule; minus an OH adsorbed on the surface (b); minus the complex with an H (c).

descriptions of energy bands of elemental materials (including transition metals) as well as compound bulk materials in various phases. It is applicable to large extended systems and provides valuable qualitative insight on the role of chemical bonding. The method is, therefore, most suitable to develop a clear chemical picture of the nature of electronic transitions and the interfacial electron-transfer mechanism.

The EH Hamiltonian of the bare and functionalized TiO_2 is diagonalized in the basis of AOs by solving the generalized EH eigenvalue problem, $HQ^q = E_qSQ^q$, where H is the EH matrix, S is the atomic orbital overlap matrix, and Q^q are the expansion coefficients of the molecular orbital (MO) with eigenvalue E_q.

The oscillator strength f of the transition with energy $E_{q'} - E_q$ is computed by using the expression $f \approx \frac{8\pi^2\bar{\nu}cm}{3he^2}\left|\langle\psi_{q'}|e\hat{r}|\psi_q\rangle\right|^2$, where $\hat{r}$ is the electronic position operator, $\bar{\nu}$ is the wavenumber of the transition, c is the speed of light, m is the electron mass, h is Planck's constant, and $\langle r|\psi_q\rangle$ is the wavefunction of the MO with eigenvalue E_q in the coordinate representation. The oscillator strengths are used to assign relative weights to the transitions and the total absorbance is globally scaled to facilitate the comparison with the experimental results. The stick-spectrum of discrete transitions is convoluted with a Gaussian function to match the experimental inhomogeneous broadening.

4. Results and discussion

Well-crystallized TiO_2 materials are usually preferred in photocatalytic applications, over amorphous materials, as photogenerated electron-hole pairs tend to recombine at defect sites on an amorphous TiO_2 surface.[43] In this study, three TiO_2 materials with different degrees of crystallinity were analyzed as substrate supports for complex **1**. P25, the gold standard for photocatalysts, was synthesized by a high-temperature (greater than 1200 °C) flame hydrolysis method.[44] X-ray diffraction data confirm P25 consists of ~85% anatase and ~15% rutile [Fig. 2(a)]. For the synthesized TiO_2 nanoparticles without further thermal treatment, a broad (101) diffraction in its XRD pattern [Fig. 2(c)] indicates that D70 nanoparticles are mainly anatase phase with a relatively low degree of crystallinity and have small particle sizes (TEM data are provided in Fig. S2†). Upon sintering at 450 °C, the anatase nanoparticles became better crystallized, as demonstrated by the narrowed (101) diffraction in Fig. 2(b) relative to that in Fig. 2(c). The BET surface areas of D70, D450, and P25 were measured to be 310, 85, and 50 $m^2\ g^{-1}$, respectively.

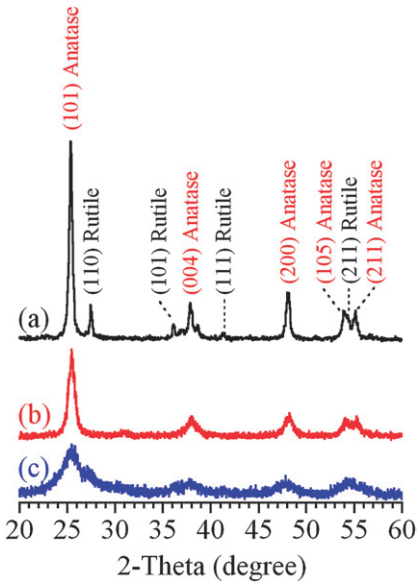

Fig. 2 Powder XRD patterns of (a) P25, (b) D450, and (c) D70.

4.1. Structural characterization of 1 deposited on TiO_2 nanoparticles

EPR data. EPR spectroscopy serves as a highly sensitive technique to detect the existence of complex **1** on TiO_2 surfaces. The mixed-valent complex **1** shows a characteristic 16-line EPR spectrum [Fig. 3(d)], that results from the hyperfine coupling between an $S = 1/2$ electron spin with two nonequivalent ^{55}Mn nuclei.[45] In the EPR spectra of **1** adsorbed on crystallized TiO_2 materials (P25 and D450), the 16 lines are barely resolved, with relatively low intensity [see Fig. 3(a) and 3(b)]. Line overlapping and broadening are also significant. This implies that only a small quantity of **1** in the mixed-valence (III,IV) state exists on the surfaces of crystallized P25 and D450 nanoparticles. However, an intense 16-line signature is seen in the EPR spectrum of **1**–D70, deposited *via* either direct adsorption or *in situ* synthesis (Fig. 3c), indicating that complex **1** containing a $Mn^{III}(\mu\text{-}O)_2Mn^{IV}$ core was anchored on the surface of near-amorphous D70 nanoparticles. The 16-line EPR spectrum of **1**–D70 did not change significantly after washing **1**–D70 with H_2O or solutions of 0.1 M $NaNO_3$ or $Ca(NO_3)_2$. Thus, complex **1** was irreversibly bound to D70 NPs. A close comparison between Fig. 3(c) and 3(d) revealed that the hyperfine coupling tensors for Mn^{III} (A_1) and Mn^{IV} (A_2) are significantly smaller for

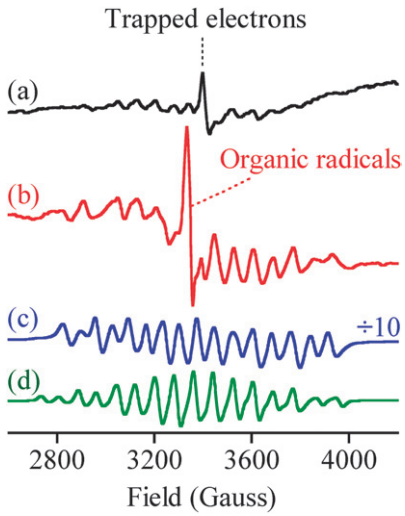

Fig. 3 EPR spectra of (a) **1**–P25, (b) **1**–D450, and (c) **1**–D70. The EPR spectrum of complex **1** in a HOAc/NaOAc buffer solution (pH 4.5) is also shown in the figure (d). A trapped electron signal and an organic radical signal are also present in spectra (a) and (b), respectively. The spectrum (c) was scaled down to 1/10 of its original magnitude to allow a better comparison.

1–D70 than for those of pure **1** (see Fig. S3†). This suggests that the Mn coordination environment was changed by binding to the surfaces of D70 NPs. As will be discussed in the DFT analysis, complex **1** may be bound to the TiO_2 surface *via* an oxo bridge Mn–O–Ti. The decrease in the hyperfine coupling tensors for **1** bound to the surface of D70 would then be explained by the replacement of a water molecule on the Mn(IV) center by an oxo group.

The photochemical behavior of **1**–TiO_2 materials was studied with EPR spectroscopy. For each sample, EPR spectra were taken in dark and under illumination with visible light (>425 nm). A difference spectrum was obtained by subtracting the dark spectrum from the one under illumination. As shown in Fig. 4(a), a resonance corresponding to trapped electrons in the rutile lattice was seen for **1**–P25 after illumination with visible

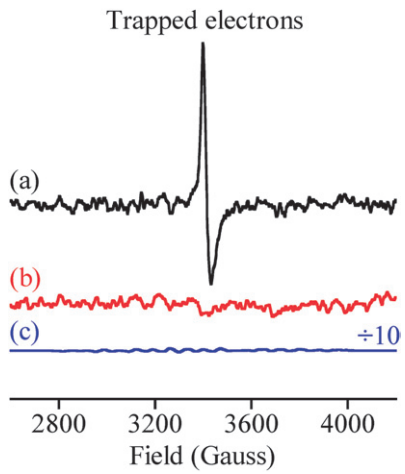

Fig. 4 Light-minus-dark difference EPR spectra measured at 7 K of (a) **1**–P25, (b) **1**–D450, and (c) **1**–D70. A resonance at g ~ 1.97, corresponding to trapped electrons in a rutile lattice, was seen for **1**–P25.

light. This signal was not seen for bare P25 under the same experimental conditions. An electron signal identical to the one shown in Fig. 3(a) was also observed for **1**–P25 prepared in complete dark conditions. Thus, the electrons may be generated in the dark and transferred to the deep trapping sites in P25. One possible process is the dimerization of **1** to form a Mn(IV) tetramer (2 Mn(III,IV) dimers form 1 Mn(IV) tetramer plus $2e^-$), as will be discussed later in the text. The lack of such trapping sites in D450 or D70 can explain the absence of an electron signal in the EPR spectra in Fig. 3(b) and 3(c), which were collected under the same conditions as the one in Fig. 3(a). Upon visible light illumination, electrons may also be liberated from the surface Mn complexes or residual, free terpy ligand on P25 and transferred to the trapping sites in P25, leading to the further increase in the rutile electron signal.

DFT analysis. As can be inferred from the EPR data, shown in Fig. 3, the Mn coordination environments in the complex **1**–D70 are different from those in the isolated complex **1**. This difference is likely due to the slightly different magnetic environment of the Mn center directly bound to the TiO_2 surface *via* an oxo bridge Mn–O–Ti. Compared to well-crystallized nanoparticles, amorphous TiO_2 materials usually contain more surface hydroxyl groups (Ti–OH) that serve as anchoring sites for complex **1**, as indicated by the QM/MM minimum energy configuration of complex **1** on the surface of TiO_2 anatase (see Fig. 1). In fact, our DFT QM/MM calculations predict that $\Delta H_b = -54$ kcal mol^{-1} is the binding enthalpy of **1** to the OH groups on the (101) surface of anatase.

The structural and electronic analysis of our QM and DFT-QM/MM models indicate that the attachment of **1** does not significantly affect the spin density of the Mn centers (*i.e.*, the spin densities change less than 5% upon attachment, from 3.83 to 3.88 a.u. for Mn^{III} and from 2.57 to 2.53 a.u. for Mn^{IV}). Structural rearrangements, however, are more significant. One of the terpy ligands exhibits a slight distortion upon adsorption of the complex, leading to an increase in the Mn^{III}–N distances. The Jahn–Teller elongation axis of Mn^{III} does not change upon adsorption of the complex, but the Mn–N distances increase (see Table 1, third row). Also, replacing a water molecule by an oxo group, that is a better electron donor, decreases the Mn^{IV}–O distance (Table 1, second row) and stabilizes the Mn^{IV} center.

UV-visible data. The optical absorption spectra of the two systems are significantly different in the UV-visible region,

Table 1 Comparison of Mn–ligand distances for **1** and **1**–TiO_2 as described by our QM and DFT-QM/MM models

	Atom–atom distances/Å	
	1	**1**–TiO_2
Mn^{III}-oxo	1.83, 1.91	1.82, 1.82
Mn^{IV}-oxo	1.73, 1.77	1.77, 1.84, 1.82
Mn^{III}–N	2.06, 2.21, 2.21	2.19, 2.28, 2.41
Mn^{IV}–N	2.00, 2.03, 2.03	2.02, 2.06, 2.06
Mn^{III}–O (of water)	2.22	2.11
Mn^{IV}–O (of water)	2.15	—

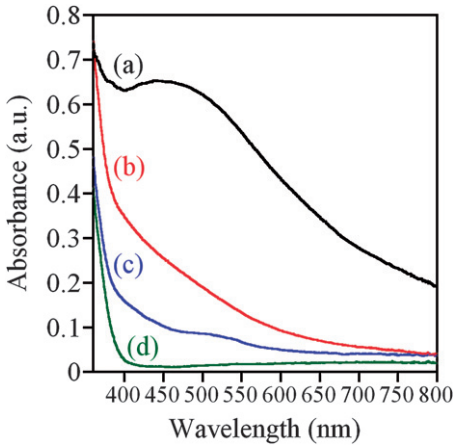

Fig. 5 UV-visible spectra of (a) **1**–P25, (b) **1**–D450, (c) **1**–D70, and (d) bare D70 NPs.

providing valuable information regarding the electronic structure of the oxomanganese surface complex on different TiO_2 materials. The UV-visible spectrum of **1**–D70 [Fig. 5(c)] resembles that of **1** in solution (see Fig. S4†).[22,33] This is consistent with the EPR results shown in Fig. 3(c), confirming the existence of a significant amount of **1** on the surfaces of D70 nanoparticles, and is also similar to the simulated UV-visible spectrum of **1**–TiO_2 shown in Fig. 6, along with the experimental spectrum of **1**–D70.

Complex **1** exhibits two prominent features in the UV-visible absorption spectrum, including one at 450 nm and the other at 650 nm, as indicated by our computational analysis and the experimental spectrum (Fig. 6 and S4†). Upon adsorption to a TiO_2 nanoparticle, the two absorption features are blue shifted to 420 nm and 610 nm, respectively. The transition at 420 nm is assigned to a ligand-to-metal-charge-transfer (LMCT) transition from the terpyridyl ligands to the manganese oxo core, while the transition at 610 nm is assigned to a terpyridyl π–π^* transition. Cross transitions from **1** to the TiO_2 surface are observed in the range 400–550 nm, although with smaller intensity.

The UV-visible spectrum of **1**–D450 [Fig. 5(b)] is not very informative, but an intense and broad absorption around 450 nm is observed for **1**–P25 [Fig. 5(a)], indicating the possible existence of an oxidized form of **1** containing a $Mn^{IV}(\mu\text{-}O)_2Mn^{IV}$ core, a Mn tetramer featuring a $Mn^{IV}(\mu\text{-}O)_2Mn^{IV}$–O–$Mn^{IV}(\mu\text{-}O)_2Mn^{IV}$ unit (see S5†),[46] or even solid-state compounds of Mn^{4+} such as MnO_2.

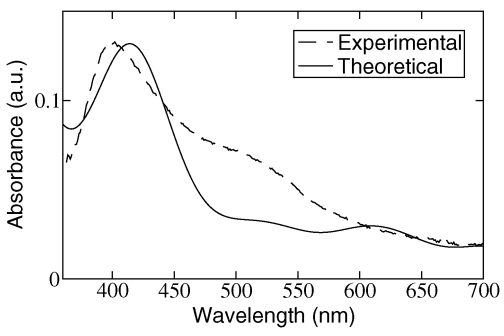

Fig. 6 Simulated UV-visible difference spectrum (solid line) compared to the experimental difference spectrum (dashed line). The difference spectrum is the spectrum of **1**–D70 [Fig. 5(c)] minus the spectrum of D70 [Fig. 5(d)]. The simulated spectrum was convoluted with gaussians with an FWHM of 60 nm to facilitate comparison.

Elemental analysis data. The elemental analysis of dried **1**–TiO_2 samples suggests that the terpy ligand was intact on the surfaces of different TiO_2 nanoparticles, since the estimated N contents based on a N/C atomic ratio of 1 : 5 are in excellent agreement with experimental results (Table 2). The results shown in Table 2 further suggest that appreciable amounts of terpy-coordinated Mn complexes may exist on crystallized P25 and D450, although the EPR results in Fig. 3 ruled out the possibility of a significant amount of **1** remaining on the surfaces of these two crystallized TiO_2 materials.

O_2 evolution data. The **1**–TiO_2 samples were also tested as catalysts for water oxidation using Ce^{4+} as the (single-electron) primary oxidant (see Fig. 7). Significant oxygen evolution is observed for **1**–P25, while mild oxygen production was seen for **1**–D450 and none for **1**–D70, suggesting that the Mn surface complexes are different in the three materials. The O_2 uptake observed for **1**–D70 and bare P25 NPs [Fig. 7(c) and 7(d)] is

Table 2 Content of C and N (weight percentages) in different **1**–TiO_2 samples

	Experimental		Calculated[a]	
TiO_2	C	N	N	**1**/μmol
P25	0.09	0.020	0.021	0.05
D450	0.11	0.021	0.026	0.06
D70	0.23	0.057	0.055	0.13

[a] Estimation based on the experimental values of C content, making the assumption that the adsorbates remain in the di-μ-oxo dinuclear form with a Mn : N : C atomic ratio of 1 : 3 : 15 when attached on the surfaces of **1**–TiO_2 materials.

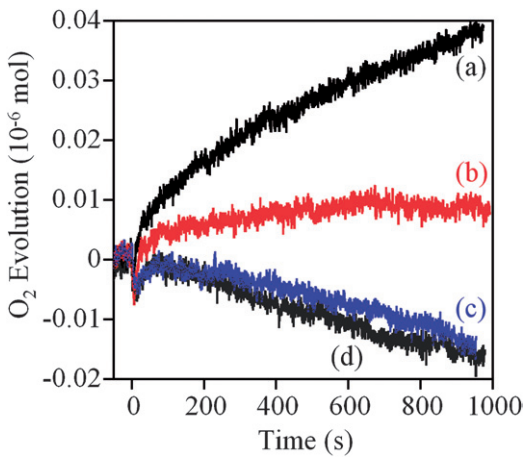

Fig. 7 O_2 evolution using Ce^{4+} as a single-electron oxidant. **1** was loaded on TiO_2 (50 mg) samples: (a) P25, (b) D450, and (c) D70. A control test was also done using (d) bare P25 NP's as the catalyst.

attributed to O_2 uptake by the Clark-type O_2 electrode under the acidic conditions of the assay. For **1**–D70, the EPR results in Fig. 3(c) show that the mixed-valence Mn(III,IV) dimer is bound to the surface in high yield. However, previous work has shown that this species is unstable in acidic Ce^{4+} solutions.[35] Therefore, we conclude that the lack of O_2 evolution activity for **1**–D70 is due to decomposition of **1**. On the other hand, previous work has shown that a Mn(IV)-terpy tetramer, $[Mn_4O_5(H_2O)_2(terpy)_4]^{6+}$ (**2**) with the connectivity of $Mn^{IV}(\mu\text{-}O)_2Mn^{IV}$–O–$Mn^{IV}(\mu\text{-}O)_2Mn^{IV}$, is formed from **1** under acidic conditions.[46,47] The observation of O_2 evolution activity for **1**–P25 and **1**–D450 [Fig. 7(a) and 7(b)] could be explained if **1** dimerizes on the TiO_2 surface to form the Mn(IV)-terpy tetramer. This would also account for the low yield of the mixed-valence Mn(III,IV) dimer EPR signal in these two samples since the Mn(IV) tetramer is EPR silent.

The loading of complex **2**, the Mn(IV) tetramer, onto P25 would be ~0.025 μmol, assuming complex **1** dimerizes on P25 (see Table 2). It can be inferred from Fig. 7(a) that ~0.04 μmol O_2 was generated after 1000 s using functionalized P25 as the catalyst. This leads to a turnover number greater than 1 for O_2 evolution, suggesting that water oxidation on functionalized P25 is catalytic. Furthermore, the initial rate of O_2 evolution is estimated to be ~0.04 nmol s^{-1}, comparable to that for complex **1** supported on clay at a loading of ~0.3 μmol as reported by Yagi and co-workers.[28]

4.3. Electrochemical characterization of 1–TiO_2

To understand the redox properties of **1**–P25 and characterize the electrochemistry of **1** on different TiO_2 surfaces, we have performed cyclic voltammetry. TiO_2 electrodes were prepared by using standard techniques, doctor-blading TiO_2 suspensions on FTO conducting glass slides and subsequently sintering them at 450 °C, before use as the working electrode in a standard three-electrode configuration. The requirement for sintering the samples at elevated temperatures before the electrochemical measurements precluded electrochemical study of **1**–D70.

The observed redox behavior of **1** on TiO_2 electrodes is similar to the redox activity previously reported for homogeneous $Mn^{III}(\mu\text{-}O)_2Mn^{IV}$ catalysts of water oxidation.[47] Our cyclic voltammograms, shown in Fig. 8, exhibit fairly well-resolved redox behavior, including a quasi-reversible redox couple centered at approximately 1 V, corresponding to $Mn^{III}(\mu\text{-}O)_2Mn^{IV}$ ↔ $Mn^{IV}(\mu\text{–}O)_2Mn^{IV}$ (P_a^1 and P_c^1).

Subsequent dimerization of $Mn^{IV}(\mu\text{-}O)_2Mn^{IV}$ can occur, forming the Mn(IV)-terpy tetramer (**2**).[47] Using the bare FTO electrode, the reduction of this tetrameric species gives a broad cathodic wave at *ca.* 850 mV (P_c^2). This cathodic current corresponding to reduction of the Mn tetramer was not observed on the P25/FTO electrode and was barely noticeable on the D450/FTO electrode [see Fig. 8(a) and 8(b)]. However, a large cathodic current is seen at *ca.* 700 mV for both P25/FTO and D450/FTO, suggesting that the Mn tetramer can be stabilized on the surfaces of crystallized NPs (P25 and D450). Thus, we conclude that the reduction of the (IV,IV,IV,IV) species to the (III,IV,IV,IV) species occurs at a more reducing potential, indicating surface stabilization of the tetramer.

These results are consistent with the observation of O_2 evolution for **1**–P25 and **1**–D450 (see Fig. 7). The acidic conditions of Ce^{4+} solutions are known to give O_2 evolution for the Mn(IV) tetramer species **2**.[48] Furthermore, the cooperative interaction of two equivalents of **1** has been previously suggested to contribute to the catalytic activity when using **1**–mica as the catalyst.[29] A similar interaction is likely to be present in the current system, where dimeric oxomanganese catalysts on the surface of the nanoparticles additionally form tetrameric species.

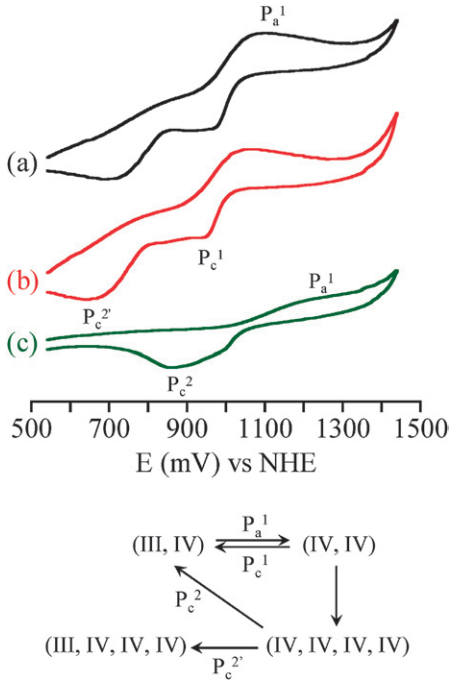

Fig. 8 Cyclic voltammograms using different working electrodes: (a) P25/FTO, (b) D450/FTO, and (c) bare FTO. The solution contained 0.57 mM **1** in 0.1 M KNO_3. Redox processes are labeled including: oxidation of $Mn^{III}(\mu\text{-}O)_2Mn^{IV}$ (P_a^1), reduction of $Mn^{IV}(\mu\text{-}O)_2Mn^{IV}$ (P_c^1), reduction of the Mn(IV) tetramer (P_c^2 and $P_c^{2'}$).

5. Conclusions

We have assembled an oxomanganese water oxidation catalyst (complex **1**) on the surfaces of near-amorphous TiO_2 nanoparticles. The **1**–TiO_2 hybrid assemblies were characterized with a variety of techniques including computational modeling, EPR and UV-visible spectroscopies and electrochemistry. Quantum mechanics calculations suggest that **1** is anchored on the TiO_2 surface *via* an oxo bridge (Mn–O–Ti), formed upon substitution of a water ligand by the surface. The mixed-valence Mn(III,IV) state of the complex **1** is not the predominant form of the surface adsorbate complex for well-crystallized TiO_2 nanoparticles, probably due to formation of a Mn(IV) tetramer. Using Ce^{4+} as a primary oxidant, oxygen evolution was observed for **1**–P25. However, the chemically-driven water oxidation was not observed for **1** in the mixed-valent form on near-amorphous TiO_2.

Our EPR measurements suggest that the formation/stabilization of a Mn(IV) tetramer from the mixed-valence Mn(III,IV) species **1** may be facilitated by irreversible electron injection into TiO_2. However, further work is required to fully

characterize the resulting surface adsorbates. Work in progress includes X-ray studies and immobilization of complex **1** by covalently attaching the complex to the TiO_2 surface by using molecular linkers. The utilization of the injected electrons, trapped in **1**–P25, and the activation of the surface catalysts with visible light will be reported elsewhere.

Acknowledgements

The authors acknowledge support from the Chemical Sciences, Geosciences, and Biosciences Division, Office of Basic Energy Sciences, Office of Science, U.S. Department of Energy (DE-FG02-07ER15909) and DOE supercomputer time from NERSC. NSF grant CHE-0215926 provided funds to purchase the ELEXSYS E500 EPR spectrometer and the NSF ECCS # 0404191 grant supported preliminary work. G.L. thanks Drs. Ping-yu Chen, Clyde Cady, Yunlong Gao, Siddhartha Das, Gerald Olack, Barry Piekos, Professor Charles Schmuttenmaer, Professor Gary Haller, Xiaoming Wang, and Gözde Ulaş for their assistance in various aspects of experiments and their helpful discussions.

References

1 A. Fujishima and K. Honda, *Nature*, 1972, **238**, 37–38.
2 T. Bak, J. Nowotny, M. Rekas and C. C. Sorrell, *Int. J. Hydrogen Energy*, 2002, **27**, 991–1022.
3 K. Rajeshwar, *J. Appl. Electrochem.*, 2007, **37**, 765–787.
4 A. L. Linsebigler, G. Q. Lu and J. T. Yates, *Chem. Rev.*, 1995, **95**, 735–758.
5 O. Carp, C. L. Huisman and A. Reller, *Prog. Solid State Chem.*, 2004, **32**, 33–177.
6 R. Asahi, T. Morikawa, T. Ohwaki, K. Aoki and Y. Taga, *Science*, 2001, **293**, 269–271.
7 X. Chen and S. S. Mao, *Chem. Rev.*, 2007, **107**, 2891–2959.
8 K. Maeda, K. Teramura, D. L. Lu, T. Takata, N. Saito, Y. Inoue and K. Domen, *Nature*, 2006, **440**, 295–295.
9 Z. G. Zou, J. H. Ye, K. Sayama and H. Arakawa, *Nature*, 2001, **414**, 625–627.
10 B. O'Regan and M. Gratzel, *Nature*, 1991, **353**, 737–740.
11 M. Gratzel, *Nature*, 2001, **414**, 338–344.
12 F. Liu, J. J. Concepcion, J. W. Jurss, T. Cardolaccia, J. L. Templeton and T. J. Meyer, *Inorg. Chem.*, 2008, **47**, 1727–1752.
13 W. Ruttinger and G. C. Dismukes, *Chem. Rev.*, 1997, **97**, 1–24.
14 N. D. Morris and T. E. Mallouk, *J. Am. Chem. Soc.*, 2002, **124**, 11114–11121.
15 J. H. Alstrum-Acevedo, M. K. Brennaman and T. J. Meyer, *Inorg. Chem.*, 2005, **44**, 6802–6827.
16 W. Lubitz, E. J. Reijerse and J. Messinger, *Energy Environ. Sci.*, 2008, **1**, 15–31.
17 M. Borgstrom, N. Shaikh, O. Johansson, M. F. Anderlund, S. Styring, B. Akermark, A. Magnuson and L. Hammarstrom, *J. Am. Chem. Soc.*, 2005, **127**, 17504–17515.
18 E. M. Sproviero, J. A. Gascon, J. P. McEvoy, G. W. Brudvig and V. S. Batista, *J. Am. Chem. Soc.*, 2008, **130**, 3428–3442.
19 E. M. Sproviero, J. A. Gascon, J. P. McEvoy, G. W. Brudvig and V. S. Batista, *J. Am. Chem. Soc.*, 2008, **130**, 6728–6730.
20 A. K. Poulsen, A. Rompel and C. J. McKenzie, *Angew. Chem., Int. Ed.*, 2005, **44**, 6916–6920.
21 R. Brimblecombe, G. F. Swiegers, G. C. Dismukes and L. Spiccia, *Angew. Chem., Int. Ed.*, 2008, **47**, 7335–7338.
22 J. Limburg, J. S. Vrettos, L. M. Liable-Sands, A. L. Rheingold, R. H. Crabtree and G. W. Brudvig, *Science*, 1999, **283**, 1524–1527.
23 J. Limburg, J. S. Vrettos, H. Y. Chen, J. C. de Paula, R. H. Crabtree and G. W. Brudvig, *J. Am. Chem. Soc.*, 2001, **123**, 423–430.
24 V. K. Yachandra, K. Sauer and M. P. Klein, *Chem. Rev.*, 1996, **96**, 2927–2950.
25 J. P. McEvoy and G. W. Brudvig, *Chem. Rev.*, 2006, **106**, 4455–4483.
26 R. Tagore, R. H. Crabtree and G. W. Brudvig, *Inorg. Chem.*, 2008, **47**, 1815–1823.
27 C. S. Mullins and V. L. Pecoraro, *Coord. Chem. Rev.*, 2008, **252**, 416–443.
28 M. Yagi and K. Narita, *J. Am. Chem. Soc.*, 2004, **126**, 8084–8085.
29 K. Narita, T. Kuwabara, K. Sone, K.-i. Shimizu and M. Yagi, *J. Phys. Chem. B*, 2006, **110**, 23107–23114.
30 W. W. Weare, Y. Pushkar, V. K. Yachandra and H. Frei, *J. Am. Chem. Soc.*, 2008, **130**, 11355–11363.
31 S. G. Abuabara, C. W. Cady, J. B. Baxter, C. A. Schmuttenmaer, R. H. Crabtree, G. W. Brudvig and V. S. Batista, *J. Phys. Chem. C*, 2007, **111**, 11982–11990.
32 W. R. McNamara, R. C. I. Snoeberger, G. Li, J. M. Schleicher, C. W. Cady, M. Poyatos, C. A. Schmuttenmaer, R. H. Crabtree, G. W. Brudvig and V. S. Batista, *J. Am. Chem. Soc.*, 2008, **130**, 14329–14338.
33 H. Y. Chen, R. Tagore, S. Das, C. Incarvito, J. W. Faller, R. H. Crabtree and G. W. Brudvig, *Inorg. Chem.*, 2005, **44**, 7661–7670.
34 G. Li and K. A. Gray, *Chem. Mater.*, 2007, **19**, 1143–1146.
35 R. Tagore, H. Chen, H. Zhang, R. H. Crabtree and G. W. Brudvig, *Inorg. Chim. Acta*, 2007, **360**, 2983–2989.
36 E. M. Sproviero, J. A. Gascon, J. P. McEvoy, G. W. Brudvig and V. S. Batista, *J. Inorg. Biochem.*, 2006, **100**, 786–800.
37 S. Dapprich, I. Komaroni, K. S. Byun, K. Morokuma and M. J. Frisch, *THEOCHEM*, 1999, **461**, 1–21.
38 M. J. Frisch, G. W. Trucks, H. B. Schlegel, G. E. Scuseria, M. A. Robb, J. R. Cheeseman, J. A. Montgomery Jr, T. Vreven, K. N. Kudin, J. C. Burant, J. M. Millam, S. S. Iyengar, J. Tomasi, V. Barone, B. Mennucci, M. Cossi, G. Scalmani, N. Rega, G. A. Petersson, H. Nakatsuji, M. Hada, M. Ehara, K. Toyota, R. Fukuda, J. Hasegawa, M. Ishida, T. Nakajima, Y. Honda, O. Kitao, H. Nakai, M. Klene, X. Li, J. E. Knox, H. P. Hratchian, J. B. Cross, V. Bakken, C. Adamo, J. Jaramillo, R. Gomperts, R. E. Stratmann, O. Yazyev, A. J. Austin, R. Cammi, C. Pomelli, J. W. Ochterski, P. Y. Ayala, K. Morokuma, G. A. Voth, P. Salvador, J. J. Dannenberg, V. G. Zakrzewski, S. Dapprich, A. D. Daniels, M. C. Strain, O. Farkas, D. K. Malick, A. D. Rabuck, K. Raghavachari, J. B. Foresman, J. V. Ortiz, Q. Cui, A. G. Baboul, S. Clifford, J. Cioslowski, B. B. Stefanov, G. Liu, A. Liashenko, P. Piskorz, I. Komaromi, R. L. Martin, D. J. Fox, T. Keith, M. A. Al-Laham, C. Y. Peng, A. Nanayakkara, M. Challacombe, P. M. W. Gill, B. Johnson, W. Chen, M. W. Wong, C. Gonzalez, J. A. Pople, Gaussian, Inc., Wallingford, CT, 2004.
39 (*a*) G. Vacek, J. K. Perry and J. M. Langlois, *Chem. Phys. Lett.*, 1999, **310**, 189–194; (*b*) E. M. Sproviero, J. A. Gascón, J. P. McEvoy, G. W. Brudvig and V. S. Batista, *J. Chem. Theory Comput.*, 2006, **2**, 1119–1134.
40 *Jaguar 5.5*; L. Schroedinger, Portland, OR, 2003.
41 A. K. Rappe, C. J. Casewit, K. S. Colwell, W. A. I. Goddard and W. M. Skiff, *J. Am. Chem. Soc.*, 1992, **114**, 10024–10035.
42 A. K. Rappe and W. A. I. Goddard, *J. Phys. Chem.*, 1991, **95**, 3358–3363.
43 G. Li and K. A. Gray, *Chem. Phys.*, 2007, **339**, 173–187.
44 A. Mills and S. LeHunte, *J. Photochem. Photobiol., A*, 1997, **108**, 1–35.
45 S. R. Cooper, G. C. Dismukes, M. P. Klein and M. Calvin, *J. Am. Chem. Soc.*, 1978, **100**, 7248–7252.
46 H. Y. Chen, J. W. Faller, R. H. Crabtree and G. W. Brudvig, *J. Am. Chem. Soc.*, 2004, **126**, 7345–7349.
47 C. Baffert, S. Romain, A. Richardot, J. Lepretre, B. Lefebvre, A. Deronzier and M. Collomb, *J. Am. Chem. Soc.*, 2005, **127**, 13694–13704.
48 Y. Gao, C. W. Cady, R. H. Crabtree, G. W. Brudvig, manuscript in preparation.

